Draft version July 7, 2022
Typeset using LaTeX **twocolumn** style in AASTeX62

arXiv:2207.02245v1 [astro-ph.GA] 5 Jul 2022

Blow-Away in the Extreme Low-Mass Starburst Galaxy Pox 186

Nathan R. Eggen,[1] Claudia Scarlata,[1] Evan Skillman,[1] and Anne Jaskot[2]

[1] *Minnesota Institute for Astrophysics, University of Minnesota*
[2] *Department of Astronomy, Williams College*

ABSTRACT

Pox 186 is an exceptionally small dwarf starburst galaxy hosting a stellar mass of $\sim 10^5$ $M_\odot$. Undetected in H I ($M < 10^6$ $M_\odot$) from deep 21 cm observations and with an [O III]/[O II] (5007/3727) ratio of 18.3 ± 0.11, Pox 186 is a promising candidate Lyman continuum emitter. It may be a possible analog of low-mass reionization-era galaxies. We present a spatially resolved kinematic study of Pox 186 and identify two distinct ionized gas components: a broad one with $\sigma > 400$ km s^{-1}, and a narrow one with $\sigma < 30$ km s^{-1}. We find strikingly different morphologies between the two components and direct evidence of outflows as seen in the high velocity gas. Possible physical mechanisms driving the creation of high velocity gas seen in [O III] are discussed, from outflow geometry to turbulent mixing between a hot (10^6 K) star-cluster wind and cooler (10^4 K) gas clouds. We find a modest mass-outflow rate of 0.022 $M_\odot$ yr^{-1} with a small mass loading factor of 0.5, consistent with other low mass galaxies. Finally we compare the mass-loading factor of Pox 186 with extrapolations from numerical simulations and discuss possible reasons for the apparent discrepancy between them.

Keywords: Dwarf Galaxies, Emission-Line Galaxies, Starburst Galaxies, Structure and Morphology

1. INTRODUCTION

1.1. *On Outlfows*

Star-formation and stellar feedback are primary ingredients in galaxy evolution, with photoionization and momentum deposition into the surrounding interstellar medium (ISM) being the main sources of stellar feedback. In a starburst large enough, the mechanical feedback can be sufficient to drive major outflows, called galactic winds, moving material into the circumgalactic medium (CGM) and intergalactic medium (IGM) beyond.

Models of galactic winds have evolved overtime. Early models predicted that winds in dwarf galaxies have a larger impact as compared to high mass systems (Dekel & Silk 1986; Mac Low & Ferrara 1999; Ferrara & Tolstoy 2000). This is due to the shallower potential wells of dwarf galaxies allowing for more easily launched winds. Since then gas removal, re-accretion of ejected material, inhibition of accreting material due to heating, mixing between gas phases in the outflow, and heating of the ISM have all been added to hydrodynamical simulations (Oppenheimer & Davé 2009; Christensen et al. 2016; Lu et al. 2017; Schneider et al. 2020). These studies have provided quantitative predictions on how winds impact galaxy properties such as stellar mass growth, and metallicity in the CGM and IGM (Christensen et al. 2018).

Verifying predictions with observations, however, is challenging due to the physical nature of winds. Galactic winds have low surface brightnesses and are transient in nature resulting from being driven by the stellar winds and resulting supernovae of the largest stars. Compounding this effect, outflows are multi-phase phenomena, requiring observations on gas temperatures ranging from 10^8 K to molecular gas at $\sim 10^2$ K to have a full picture. As a result seemingly simple properties of outflows, for example their radial extent, have still not been observationally measured.

Each phase of the outflow has its own characteristics. The hot phase of the outflow ($T > 10^6$ K) typically contains $\sim$10% of the mass (Kim et al. 2017), but has the highest velocity and likelihood of reaching the IGM ($v > 1500$ km s^{-1}). It also tends to be metal enriched, being made up of supernova ejecta and thermalized stellar winds. Most mass tends to be contained in the warm phase ($T \sim 10^4$ K). The warm phase consists of ionized gas in the ISM swept up by the outflow, cooler shock-heated gas, and condensed gas that cooled out of the

eggen091@umn.edu

hot phase. It tends to have lower velocities than the hot phase (v ∼500-1000 $\mathrm{km\,s^{-1}}$) and, depending on the galaxy, can also reach the CGM and IGM. Finally the cold neutral gas phase (T<10^3 K) has been found to be ubiquitous in galactic outflows of high mass galaxies, making up as much as 50% of the outflowing mass in the most extreme cases. In models of dwarf galaxies, however, the cool phase mass is subdominant to the warm phase (Hopkins et al. 2012; Oñorbe et al. 2015; Christensen et al. 2016; Hu 2019; Nelson et al. 2019).

The warm phase tends to be the easiest phase to observe due to the plethora of nebular lines emitted by the gas in the optical, but care must be taken to separate the emission in the outflow from the host galaxy. This disentanglement turns out to be a major problem. Simple imaging of the outflowing gas is dubious, where nebular lines from the outflow are dominated by the starburst in the host galaxy. With kinematic information the high velocity gas can be isolated, but long-slit and multi-object spectrographs may provide only partial spatial information. Integral field spectroscopy therefore is a natural solution for the study of outflows, providing both spectral and spatial information simultaneously. Even so, projection effects complicate the interpretation of the data. Despite these challenges, it is possible to learn much about galactic winds.

A common method of comparison between outflows of different galaxies and simulations is to measure the mass outflow rate ($\dot{M}$) relative to the star formation rate (SFR). This quantity is known as the mass-loading factor ($\eta = \dot{M}/\mathrm{SFR}$) and is a measure of the efficiency of the outflow. Observations have found mass-loading factors ranging widely, from less than 1 to greater than 50 in the most extreme cases (Martin 1999; Heckman et al. 2015; Chisholm et al. 2017). Simulations also find widely varying mass-loading factors (Muratov et al. 2015; Christensen et al. 2016; Hu 2019; Nelson et al. 2019), but where observations are conflicting if there is a trend between stellar mass and mass-loading factor, simulations agree, finding galaxies with lower stellar masses driving more efficient outflows (McQuinn et al. 2019).

Variations in mass-loading factors between galaxies are to be expected. The timescale intrinsic to the method of measuring mass-outflow rates gives an instantaneous snapshot of the outflowing material. Star-formation rates, however, measure the amount of star formation over the last few 10s of Myrs, during which time an outflow and the instantaneous SFR can evolve significantly. This difference in timescale can manifest as changes in measured mass-loading factors depending on the specific scenario in a given galaxy. A simple case is the difference between an instantaneous starburst and continuous star-formation. The instantaneous starburst would be expected to produce a more powerful outflow from the focused feedback, but the measured SFR would be the same. Another interesting scenario that would affect the mass-loading factor is an ISM blow-away, where a significant fraction of the ISM is removed from the galaxy through feedback[1]. If $\dot{M}$ is measured a sufficiently long time after the initial burst of star-formation to allow the blow-away to occur, then there would be less gas remaining to be "loaded" into the outflow, and the mass outflow rate would be suppressed.

1.2. *Outflows, Reionization, and Green Pea Galaxies*

Outflows are also important in the context of escaping ionizing radiation from the host galaxy. The low-density, highly ionized channels created by outflows in the ISM are ideal environments for ionizing radiation to escape, which is a major problem in the study of reionization.

Low mass star-forming galaxies are thought to be the primary sources of ionizing photons during the epoch of reionization (Livermore et al. 2017; Steidel et al. 2018; see Naidu et al. 2020 for an alternative model). A galaxy's capacity to contribute to reionization depends on the total ionizing flux produced and the fraction that escapes its interstellar medium (f_{esc}), reaching the intergalactic medium (IGM, Robertson et al. 2015). For reionization to complete by z∼6, *all* galaxies must have had an average escape fraction between 10-20% (Finkelstein et al. 2015; Robertson et al. 2015) or the ionizing photon production efficiency must be higher than previously assumed (Finkelstein et al. 2019).

An increasingly opaque IGM, however, makes direct observations of these galaxies' escaping ionizing flux difficult. Beyond z∼4, the number of neutral hydrogen cloud absorbers becomes large enough to inhibit direct observations of ionizing flux. Observations have found the evolution with redshift of the number of absorbers above a certain column density can be described as a broken powerlaw (Sargent et al. 1980; Young et al. 1982b; Zuo & Lu 1993), with the exponent increasing from 2.82 to 5.07 at $z > 3.11$. With such a sharp increase in the number of absorbers at high redshift, determining the amount of ionizing radiation an object emits is increasingly difficult to reconstruct from the amount of ionizing radiation that reaches an observer. Therefore, a set of observables that indicate high escape fractions but are also accessible at z> 6 is needed to further constrain the escaping ionizing flux from galaxies responsible for reionization.

[1] We adopt the definitions from Mac Low & Ferrara 1999 when referring to blow-outs and blow-aways.

Galaxies with high escape fractions have been found among low redshift analogs, notably the so-called "Green Peas" (GPs, Cardamone et al. 2009). Selected for their high [O III]/[O II] (5007/3727; O_{32}) ratio, Green Peas are compact, highly star-forming galaxies similar to those responsible for reionization. Some Green Peas have been found with escape fractions as high as 70% (Izotov et al. 2016a,b; Schaerer et al. 2016; Verhamme et al. 2017) and a strong anti-correlation between the separation of Lyman alpha peaks and f_{esc} has been observed (Izotov et al. 2018b), implying gas kinematics and structure play an important role in determining f_{esc}. Lyman alpha's resonance, however, makes its line-shape difficult to interpret. In addition, Green Peas are limited as useful analogs if indeed low-mass galaxies dominate reionization. They are many times more massive than these galaxies (e.g., Weisz & Boylan-Kolchin 2017) while simultaneously being too compact and far away (z∼0.3) to be structurally studied in detail. Looking locally (z∼0) allows for the mapping of gas kinematics in galaxies with properties analogous to Green Peas, and masses similar to galaxies thought to be responsible for reionization. Here we examine one such galaxy, Pox 186.

1.3. *Pox 186*

Pox 186 was originally discovered as an emission line, Blue Compact Dwarf (BCD) galaxy in the objective prism survey of Kunth et al. (1981). The special character of Pox 186 was highlighted by Kunth et al. (1988), whose ground-based imaging showed no evidence of an underlying stellar population associated with the starburst and reported Pox 186 as a non-detection in a dedicated search with the Nancay radiotelescope for H I 21cm emission. These two characteristics, having a starburst with no apparent host galaxy and the presence of efficient star formation in the absence of a neutral gas ISM are exceptionally rare, if not unique. We hypothesize that the current starburst in Pox 186 may have resulted in the complete blow-away of its neutral ISM. In this scenario, the ionized gas that we observe today is density bounded due to the lack of a surrounding neutral ISM, and, as a result, Pox 186, like a green pea galaxy, would be expected to have a relatively high escape fraction of ionizing photons.

Pox 186 has similar characteristics to Green Pea galaxies, in particular their density bound nature with the implication that they are optically thin to Lyman continuum radiation (Jaskot et al. 2013). Three observations point to Pox 186 being density bounded, where there is not enough material in the galaxy to absorb all ionizing radiation. If entirely density bounded, f_{esc} could reach close to 100% and it would be the first case of a complete neutral gas blow-out observed in a galaxy.

First, Pox 186 has an $O_{32}>$ 20 (Guseva et al. 2004, referenced as G04 from now on), one of the most extreme values among the Green Pea sample (Izotov et al. 2017). This implies a high ionization state in the majority of the ISM.

Second, its S/O abundance ratio inferred from a standard nebular abundance analysis is ∼2 times larger than the mean for BCDs (G04), which likely stems from an overestimated ionization correction factor (ICF). This is most easily understood if the H II region is density-bounded and inappropriate ionization corrections derived from ionization-bounded H II region models are used. Sulfur's ICF is dependent on O/O^+, which is sensitive to the low ionization region at the edge of the H II region as O^0 has a similar ionization potential to neutral hydrogen. A density bounded nebula does not have the layer of low ionization at the edge of the nebula. This decreases the abundance of O^+ relative to O relative to a ionization bounded nebula, therefore increasing O/O^+ and causing an over-correction.

Finally Pox 186 remains undetected in H I 21cm, despite attempts from multiple observatories (Nancay Radio Telescope, Kunth et al. 1988; Giant Metrewave Radio Telescope, Begum et al. 2005; Very Large Array[2]). With a 5σ upper limit of $M_{HI} < 1.6 \times 10^6$ $M_\odot$, its M_{HI}/L_B ratio is ~ 0.1, much lower than that for typical BCDs (~ 1), suggesting a large portion of the H I has been ionized.

In their modeling of feedback in dwarf galaxies, Mac Low & Ferrara (1999) distinguish between blow-out, when material is ejected from the galaxy's gravitational potential and blow-away, when the entire ISM is driven away from the galaxy. If complete neutral-gas blow-away is indeed possible in a galaxy, one would expect the host galaxy to be low mass, and Mac Low & Ferrara (1999) found that only galaxies with gas masses $\leq 10^6$ $M_\odot$ were expected to be vulnerable to complete blow away. Observations and simulations of galactic outflows support this, finding low mass galaxies form galactic outflows more efficiently due to a shallow potential well (Chisholm et al. 2017; Andersson et al. 2020).

Hosting a stellar mass of $\sim 10^5$ $M_\odot$ (Corbin & Vacca 2002), Pox 186 contains less mass in stars than typical BCDs or even individual star-forming clumps in massive star-forming galaxies (Genzel et al. 2011), and is more comparable to giant H II regions (e.g., NGC 604; Yang et al. 1996). It is extremely rare to observe a

[2] John Cannon, Private Communication

Pox 186 Basic Properties

Parameter	Value	Reference
RA (deg)	201.452767	
DEC (deg)	-11.610494	
m_V (mag)	17.43 ± 0.03	1
$\log(M_*/M_\odot)$	5	2
$\log(M_{HI}/M_\odot)$	< 6.2	3
SFR ($M_\odot$/yr)	0.045 ± 0.003	2
Hβ EW (Å)	375.0 ± 0.6	1
[O III]/[O II] (O_{32})	18.3 ± 0.11	1
12 + log(O/H)	7.74 ± 0.01	1
Distance (Mpc)	13.1	4,5

Table 1. Properties of Pox 186. References are 1 (Guseva et al. 2004), 2 (Corbin & Vacca 2002), 3 (Begum et al. 2005), 4 (Shaya et al. 2017) , and 5 (Kourkchi et al. 2020).

dwarf galaxy with stellar mass less than 10^6 $M_\odot$ hosting a starburst. Thus, Pox 186 falls in a mass regime where the effects of feedback have rarely been studied observationally. Pox 186 is unique in this regard as it is simultaneously low mass, hosts a young super star cluster, and is nearby (D≈13 Mpc) allowing for spatially resolved analyses.

Pox 186 exhibits a radial velocity of $\sim$ 1200 km s^{-1}. At this redshift, nearby mass concentrations such as the Virgo Cluster, the Great Attractor, and the Shapley Concentration cause significant deviations from the Hubble flow. Therefore, we use Cosmicflows-3 (Shaya et al. 2017; Kourkchi et al. 2020) to calculate a distance of 13.1 Mpc to Pox 186. We adopt this distance and convert previous literature values using this distance for direct comparison. The distance and other parameters of Pox 186 are collected and presented in Table 1.

In this paper we present new Gemini Integral Field Spectroscopy (IFS) data to measure kinematic properties of the ionized gas across Pox 186 and explore the different mechanisms that can drive the observed nebular emission. Section 2 describes the data and reduction process while the results are shown in Section 3. The discussion and conclusions are presented in Sections 4 and 5.

2. DATA AND METHODS

2.1. *Observations*

Data were taken with Gemini-South using the Gemini Multi Object Spectrograph (GMOS) IFU over five, 1000 second exposures on April 14, 2018. We used the one slit mode, with a field of view of 3″× 5″ (corresponding to a physical scale of 196 pc × 325 pc; Figure 1), and the B600 grating for an effective wavelength range from 3650 Å to 6600 Å. The spectral resolution was $\sim$ 1.6 Å (FWHM) and seeing was 0.″88. Standard star LTT3864 was observed for flux calibration and spectra of a CuAr comparison lamp for wavelength calibration.

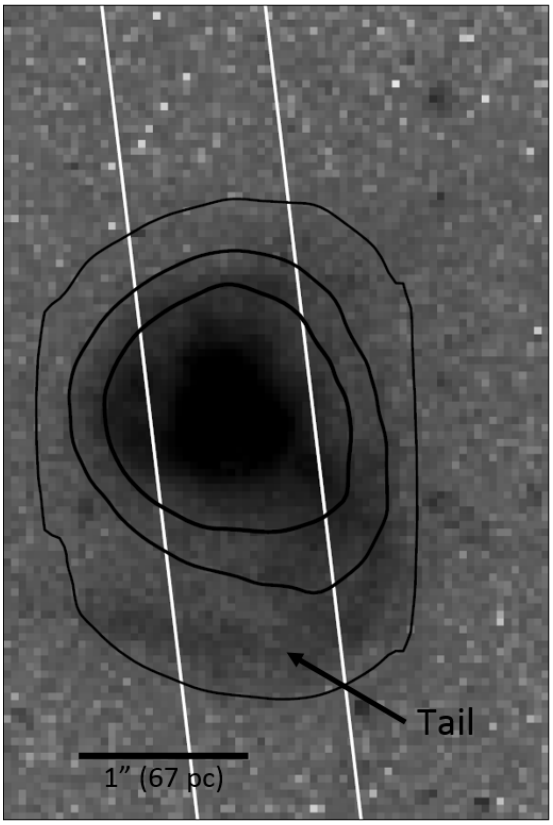


Figure 1. HST F555W image of Pox 186. The black contours denote [O III] S/N ratios of 24, 25, and 26 from the Gemini data cube while the white lines show how the slit from G04 lines up with the field of view of the data cube. The horizontal black line represents 1″. For reference 1″ corresponds to a linear scale of 67 pc.

The data are reduced primarily using Gemini's provided IRAF software package. The package includes bias and overscan subtraction, flat fielding, cosmic ray removal, wavelength calibration, scattered light and quantum efficiency corrections, fiber tracing and extraction, sky subtraction, flux calibration, and mapping each fiber into the data-cube. Due to the unreliability of the overscan and scattered light modeling routines, custom scripts in python were written and used instead. Bad columns were masked by hand before the reduction process, and the final data-cube products of each exposure were aligned by cross-correlating the images of the brightest nebular lines. The aligned data-cubes were then combined using a custom script written in python. Finally, a foreground Galactic extinction correction of $E(B-V) = 0.0385$ was applied to all spectra using the optical extinction curve from Schlafly & Finkbeiner

(2011) assuming an R_V value of 3.1. This very low correction for foreground Galactic extinction is expected due to the high Galactic latitude of +50.4° for Pox 186.

The CCD array used to take the data is an array of 3 chips, each with 4 amplifiers for 12 amplifiers total. The chip covering the red part of the spectrum experienced a charge transfer inefficiency problem for a time that included when the data were taken. This problem made data beyond $\lambda > 5450$ Å unusable. Therefore, we do not consider any lines beyond $\lambda > 5450$ Å. In addition, variation between exposures is larger than the calculated errors provided by the pipeline. Comparing line fluxes across the 5 different exposures we find a 1σ scatter of $\sim 3.8\%$. We therefore increase the error estimate by an amount of 3.8% of the flux to account for this scatter.

To be free from the uncertainty of the atmospheric transmission during the standard star observations, we calibrate our data to HST archival Wide Field Planetary Camera 2 F555W observations (HST-GO-8333, PI = Corbin; Corbin & Vacca 2002). We simulate a F555W observation using the IFU data by calculating the mean flux density over the F555W bandpass using

$$f_\lambda(P) = \frac{\int P(\lambda) f_\lambda(\lambda) \lambda d\lambda}{\int P(\lambda) \lambda d\lambda} \quad (1)$$

where $f_\lambda(\lambda)$ is the flux density and $P(\lambda)$ is the filter throughput at each wavelength. We find a factor of 3 discrepancy between our standard star flux calibrated data and HST photometry. After correcting for this discrepancy, we then compare the measured line fluxes to G04, finding good agreement within the errors.

Balmer ratios were examined to correct for the extinction from the host galaxy. As Hα fell on the CCD chip with the charge transfer inefficiency, it was not considered for this correction. We find both Hδ/Hβ and Hγ/Hβ to be consistent with Case B within the uncertainties, 0.254±0.014 and 0.488±0.025 (as compared to the theoretical values of 0.263, and 0.474) respectively.

This inferred very low extinction is expected for a low-metallicity galaxy, but the literature values for the extinction to Pox 186 show some inconsistencies. The original spectroscopy of Kunth et al. (1981) reported an Hα/Hβ ratio of 3.3, which converts to an E(B-V) of 0.15, and Kunth & Sargent (1983) derived a value of c(Hβ) = 0.39, which translates to an E(B-V) of 0.27. Corbin & Vacca (2002) report a value of E(B-V) = 0.28, in agreement with the larger of the two values. From two independent measurements, Guseva et al. (2004) report lower values of C(Hβ) = 0.02 and 0.16 (E(B-V) equivalents of 0.014 and 0.11, respectively). Although the very high value of Corbin & Vacca (2002) does not take into account underlying stellar absorption and that the Hα emission is blended with [N II] emission, and both of which would tend to overestimate the extinction, both of these effects are estimated to be at the level of 1% in flux, and so are unlikely the cause for the discrepant high value of extinction. Because our derived value for extinction is consistent with zero, we expect a low value of extinction due to the low metallicity of Pox 186, and our measurement agrees with the value obtained with the MMT by Guseva et al. (2004), we do not perform a correction for internal extinction for Pox 186. This choice has essentially no impact on any of our later conclusions.

Using 19 emission lines with the highest signal to noise we derive a spectroscopic redshift of $z = 0.00409 \pm 0.00006$, consistent with G04, who measure a redshift of $z = 0.00413 \pm 0.00005$.

2.2. *Kinematic Component Fitting*

Broad wings are prevalent in the strongest emission lines ([O III] and Hβ; Figure 2), suggesting multiple kinematic components may be present in the ionized gas of Pox 186. Spectroscopic lines from the CuAr comparison lamp are well described by a single Gaussian (S/N > 50) and therefore a nonlinear component in the instrument response cannot be responsible for the broad wings. To quantify the wings (also referred to as the "broad component"), we fit a multi-component emission line model to the [O III] doublet using Markov Chain Monte Carlo (MCMC) fitting.

We use the python implementation emcee (Foreman-Mackey et al. 2013) for our MCMC fitting using 100 walkers and iterating over 5000 steps, with the first 500 as the burn in phase. To ensure our continuum measurement is not being contaminated by the broad component we measure the continuum from $4780 - 4840$ Å. Our model uses uniform priors spanning all possible values for the parameters. [O III] 4959 Å and 5007 Å are fit simultaneously by keeping the line center offsets and Gaussian widths consistent between the two while scaling the amplitude by their intrinsic ratio, 2.94 (Osterbrock & Ferland 2006).

The narrow component is well described by a Gaussian distribution while the wings are not. First, to characterize the width of the wings in a self-consistent manner, we fit a two Gaussian model using the MCMC routine described above. After each spatial pixel (spaxel) is fit, the broad component flux S/N is evaluated as a proxy for the quality of the overall fit. The uncertainties derived from the distribution of walkers from the MCMC fit are used to measure the S/N of the flux. Spaxels with a broad fit with a S/N < 3 are then refit with a single

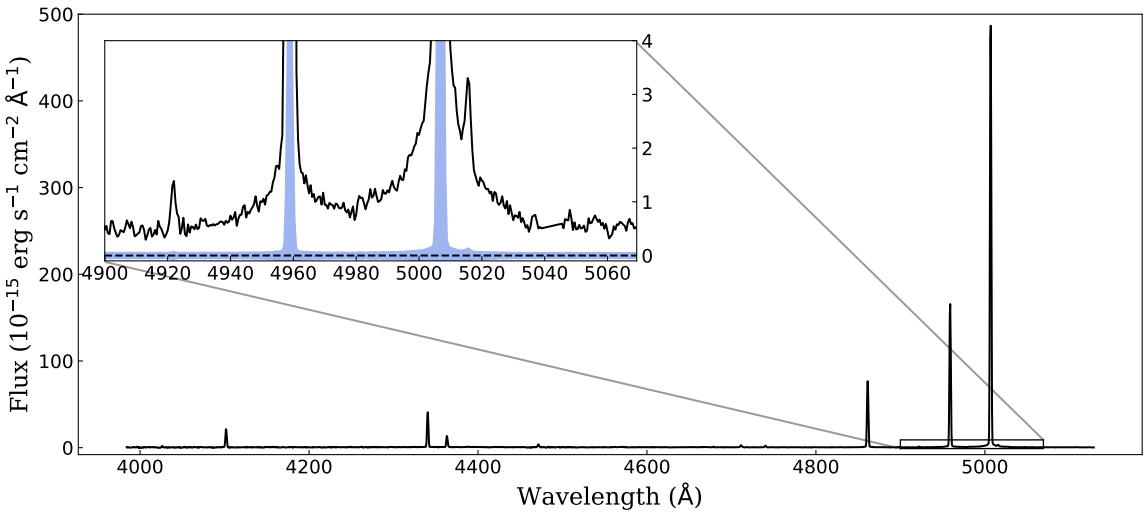


Figure 2. One dimensional spectrum. The black line is the spectrum while the blue shaded region represents the 1σ errors including the additional 3.8% of the flux as mentioned in Section 2. The zoomed in region shows the very broad wings present on the [O III] emission lines.

Gaussian model. Note that we mask out the faint He I (5016 Å) line blended with the wing of 5007 Å and He I (4922 Å) during the likelihood maximization.

Velocity dispersions of each kinematic component were corrected for thermal broadening and the instrument response, $\sigma_{int} = \sqrt{\sigma_G^2 - \sigma_T^2 - \sigma_R^2}$, where σ_G is the fit dispersion of one of the Gaussian components, σ_T is the thermal broadening, and σ_R is the velocity width of a spectral resolution element. Thermal broadening was measured from the electron temperature assuming a Maxwell-Boltzmann distribution: $\sigma_T = \sqrt{3kT_e/m}$ where m is the mass of a doubly ionized oxygen atom and T_e is the electron temperature measured with the direct method ([O III] 4363 Å and [O III] 4595 and 5007 Å) using equation 5.4 from Osterbrock & Ferland (2006). Electron temperatures derived from [O III] 4363 Å weakly depend on the electron density. As we do not detect [O II], the data exclude the [S II] doublet, and the [Ar IV] doublet traces more highly ionized gas than [O III], we assume an electron density of 350 cm^{-3} as measured by G04. Summing all spaxels into one spectrum we measure $T_e = 16780 \pm 470$ K, while the average T_e across spaxels with a 3σ detection of [O III] (4363Å) is 16920 K with an RMS scatter of 450 K. For reference G04 measure a temperature of 16940 ± 60 K. Finally, the spectral resolution, σ_R, is measured empirically from the arc lamp exposures to be 41 km s^{-1}.

3. IONIZED GAS KINEMATICS IN POX 186

We find the broad component is not detected in all spaxels. Indeed, mapping [O III] according to its radial velocity shows a transformation in geometry (Figure 3). At the line center (red shaded region and upper-middle image), the emitting gas has a circular geometry, similar to the continuum image but with an extended "halo" around the bright core. This halo is likely the low surface brightness component identified in G04 detected out to large radii (r∼6″) in ionized gas. Like G04, we find no evidence of stellar continuum at larger radii. The surrounding radial velocity slices of Figure 3 highlight the transformation from a circular geometry to elongated at high radial velocities.

MCMC Fit Parameter	Median Uncertainty	σ_{err}
Narrow Velocity Offset	1.05	1.85
Narrow Velocity Width	0.84	1.85
Broad Velocity Offset	92.9	89.3
Broad Velocity Width	98.5	223.9

Table 2. Median error and 1σ width of the distribution of errors for the each fit parameter. All values listed are in units of km s^{-1}.

This elongated geometry of the high velocity gas is seen in the results of the MCMC fits, shown in Figure 4. Spaxels where the S/N in the component's flux is less than 3 are cut out of the maps. This cut is relevant only for the broad component as the narrow component is detected with a S/N > 3 in all spaxels. The black contours are the same as in Figure 1, corresponding to S/N contours in total [O III] flux of 24, 25, and 26, and are included to help guide the eye. Table 2 list the general properties of the uncertainties in the parameters shown in Figure 4. The second column lists the median uncertainty, and the third column lists the 1-σ width of the distribution of uncertainties of the spaxels shown (σ_{err}).

The top two panels of Figure 4 show maps of the velocity offset and velocity width of the narrow component. Velocity offsets are measured as $v_{off} = c\Delta\lambda/\lambda_0$, where c is the speed of light, $\Delta\lambda = \lambda_f - \lambda_0$, and $\lambda_0 = 5006.84(1+z)$ while the velocity widths (v_w) are measured as $v_w = c\sigma_f/\lambda_0$, where σ_f is the standard deviation of the Gaussian component. In the upper half of the field of view of the velocity offset map, there is a feature of the narrow component with a small (~ 6 $\mathrm{km\,s^{-1}}$) systematic velocity shift, indicating a flow of gas that appears to originate in the core of the galaxy. There also seems to be a small gradient between the upper and lower halves of the field of view that could be evidence of rotation. The amplitude of the gradient is $\sim$2 $\mathrm{km\,s^{-1}}$ and is consistent with what one would expect of a galaxy the size of Pox 186, but is also comparable to the mean uncertainty in the velocity offsets (Table 2).

The velocity width map of the narrow component shows a small enhancement (~ 17 $\mathrm{km\,s^{-1}}$) in the tail region while the top and bottom of the field of view show larger enhancements (~ 22 $\mathrm{km\,s^{-1}}$) relative to the central region of the galaxy (~ 11 $\mathrm{km\,s^{-1}}$).

Similarly, velocity offsets and widths of the broad component are shown in the bottom two panels of Figure 4. A region of gas with a systematic velocity shift similar to the narrow component is also present in the broad component velocity offset map. The projected spatial location and amplitude of the offset are slightly different from the narrow component, but the map is limited in its usefulness due to the offset uncertainties. The offset uncertainty properties of the broad component in Table 2 highlight that outside the central $0.5''$ of the galaxy, the fit offset of the broad component is consistent with 0.

Unlike the broad offsets, the increase in width at larger radii is not a function of the fit uncertainty. The uncertainties in kinematic parameter fits are shown in the Appendix. Figure 7 shows the uncertainties follow a different distribution than the fit broad velocity widths. The broad component width increases smoothly with increasing distance from the core of the galaxy, with an asymmetric gradient where the width increases faster in the vertical directions than horizontal. Conversely the uncertainties of the broad component widths are consistently small except for the very edges of the wing region, due to the decrease in the S/N of the broad component. In addition, there is a similar level of correspondence between the narrow and broad velocity widths as there is in the offset maps. While there is no observed enhancement in the tail region that passes the S/N cut, the general increase in both component widths at increasing radii suggests some level of interaction between the narrow and broad component gas.

We find the wings are better fit by a Lorentzian profile convolved with the instrument response as compared to a Gaussian (Figure 5). The Lorentz profile fit to the wings of [O III] have a FWHM of 884 $\mathrm{km\,s^{-1}}$ and account for $7.6 \pm 0.1\%$ of the total flux of the line. Even binning all spaxels where the broad component is detected in [O III], the broad component of Hβ has a large uncertainty, accounting for $6.5 \pm 3.8\%$ of the total line flux and is slightly narrower, with a FWHM of 760 $\mathrm{km\,s^{-1}}$.

4. OUTFLOW PROPERTIES

4.1. *Outflow Rates*

Ionized gas emission is observed at extremely large velocities ($|\mathrm{v}| > 1000$ $\mathrm{km\,s^{-1}}$) but gas at large velocities does not necessarily imply an outflow. To determine if the high velocity gas constitutes an outflow, the escape velocity (v_{esc}) is estimated following Marlowe et al. (1995), who assume a spherically symmetric isothermal potential and a cutoff at r_{max}. The escape velocity at radius r becomes:

$$v_{esc} = \sqrt{2} v_{circ} \sqrt{1 + ln(r_{max}/r)} \tag{2}$$

where, for Pox 186, r_{max} is taken to be 100 pc ($1.5''$), and r to be $1/2\ r_{max}$. v_{circ} is the circular orbital velocity estimated by the virial theorem: $v_{circ} = \sqrt{GM_{tot}/r_{max}}$. The total mass is estimated by assuming a dark matter fraction of 90%, making M_{tot}=M_{baryon}+M_{DM}. M_{baryon} is the baryonic mass component and consists of stellar mass, molecular, neutral, and ionized gas masses.

The ionized (H II) mass is given by:

$$M_H = \frac{\mu m_H \lambda_{H\beta} L_{H\beta}}{hc\alpha^{eff} n_e} \tag{3}$$

where μ is the atomic weight, m_H is the mass of hydrogen, $\lambda_{H\beta}$ is the wavelength of Hβ, $L_{H\beta}$ is the luminosity of the Hβ line, h is Planck's constant, c is the speed of light, and α^{eff} is the recombination coefficient for Hβ. We take μ to be 1.36 to account for an assumed 10% He fraction, and α^{eff} to be 1.61×10^{-14} $\mathrm{cm^3\ s^{-1}}$ assuming case B recombination in 20000 K gas (Osterbrock & Ferland 2006). Using this equation we measure an H II mass of $5.4 \pm 0.38 \times 10^4$ $\mathrm{M_\odot}$. We then take the stellar population synthesis model from Corbin & Vacca (2002) which found the central star cluster to have a $\mathrm{M_*} \sim 10^5$ $\mathrm{M_\odot}$, adjust the limit on the H I mass from Begum et al. (2005) for the cosimicflows-3 distance to $\mathrm{M}_{HI} < 8.0\times10^5$ $\mathrm{M_\odot}$, and assume the neutral and molecular masses to be comparable to the neutral hydrogen mass upper limit,

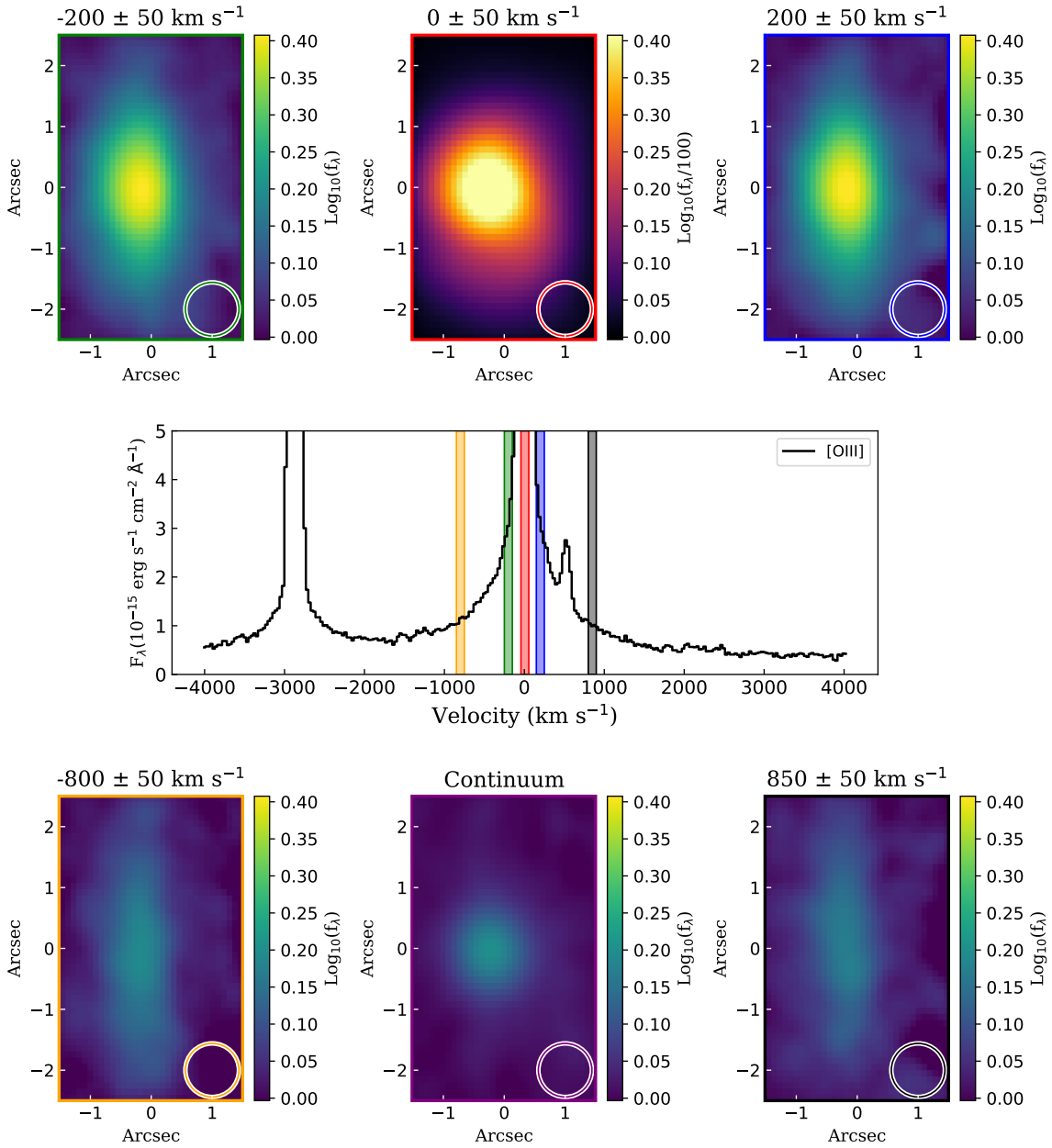


Figure 3. Flux distributions from gas at different velocities. The central panel shows the 1-dimensional spectrum summed over all spaxels while the shaded bars signify the regions in velocity space used to create the surrounding images. Each outer image has been continuum subtracted except for the continuum image. The colors of the bars match the outline of their corresponding image as well as the circle visible in the bottom right corner of each. The diameter of the circle denotes the full width half max of the seeing, .88″. The upper central panel has been scaled by 100.

$\sim 8 \times 10^5$ M$_\odot$. With these assumptions we estimate the upper limit on the total mass of Pox 186 to be 1.8×10^7 M$_\odot$ and on the escape velocity to be ~ 55 km s^{-1}. The ionized gas mass being comparable to the stellar mass is significant, and could be further evidence for a possible blow-out of the neutral gas. It is also worth noting the assumptions made above are all made conservatively to maximize the total mass and therefore escape velocity, making these values upper limits. Considering the radial velocities observed in the ionized gas are an order of magnitude greater than the upper limit on the escape velocity, it is very likely that most of the high velocity wind is not bound to Pox 186 and will escape into the IGM.

Next, the mass outflow rate of the ionized phase of the outflow is estimated. The ionized gas mass of the outflow can be measured from the total flux in the broad component assuming the entire component is high ve-

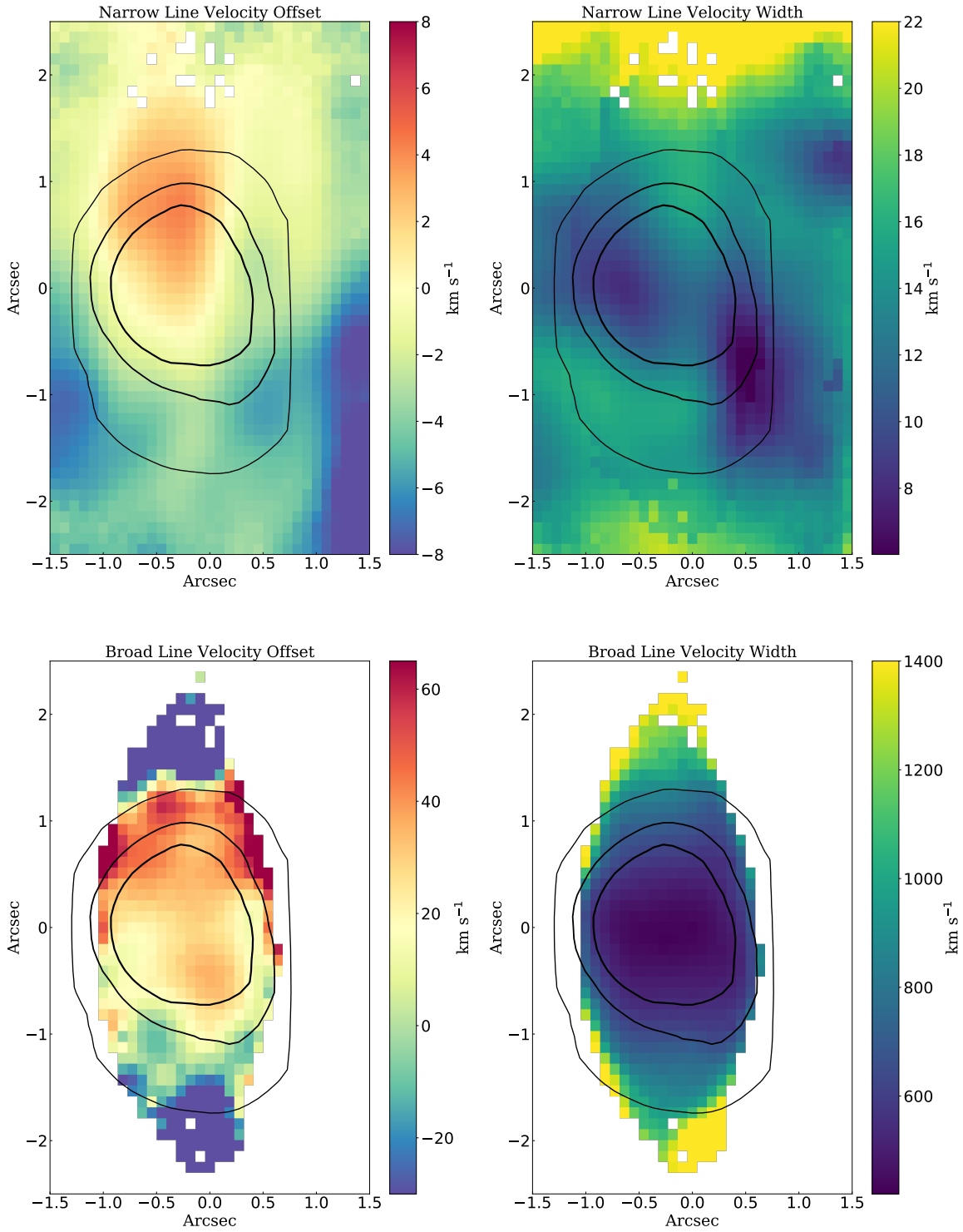


Figure 4. Kinematics of the two Gaussian components as fit by two-Gaussian model described in Section 2. Velocity dispersions are corrected for thermal dispersion and instrument response. Black contours are the same as shown in Figure 1.

locity gas that will escape the galaxy. Spaxels where the broad wings are statistically significant (S/N > 3) are summed into one spectrum to provide the highest possible S/N in the wings. A Lorentzian profile is then fit to the wings finding the broad component contributes 6.5 ± 3.8 % to the total Hβ line flux, which we refer to as the "flux fraction". Using equation 2 gives an ionized gas mass of 6.4±3.7 × 10^3 $M_\odot$ in the broad component. Equation 2 can be modified to find the mass outflow rate of the wind by multiplying by the flux fraction (F_{broad}/F_{line}) and dividing by the time it takes the wind to move through the length of the outflow (R_{out}/V_{out}):

$$\dot{M} = \frac{\mu m_H \lambda_{H\beta}}{hc\alpha^{eff} n_e} L_{H\beta} \frac{F_{broad}}{F_{line}} . \frac{V_{out}}{R_{out}} \quad (4)$$

Assuming the characteristic length of the outflow (R_{out}) is 100pc (1.5″), the outflow velocity is 450 km s^{-1} (V_{out}), and the flux fraction is 0.065, we calculate a mass outflow rate of 0.016 ± 0.010 $M_\odot$ yr^{-1}. It is worth noting the dominant source of error is the uncertainty in the flux fraction from the fitting routine. If instead of using Hβ we use the brighter [O III](5007 Å) flux fraction we calculate $\dot{M}$=0.019±0.001 $M_\odot$ yr^{-1}.

4.2. *Mass-Loading Factor*

The mass-loading factor measures the efficiency of the outflow by normalizing the mass outflow rate by the star formation rate (SFR). We follow the description in Kennicutt (1998) and correct it to use the Hβ luminosity to derive the SFR in Pox 186. Doing so, we find a SFR of 0.024 ± 0.003, corresponding to a mass-loading factor of 0.67 ± 0.42. As before, the dominant source of uncertainty results from the fitting routine. Adopting the [O III] flux fraction and uncertainty results in a mass-loading factor of 0.8 ± 0.1. We emphasize the numbers derived above are estimates. Outflows are multiphase phenomena, and the assumption that the entire broad component is high velocity gas that will escape the galaxy is not necessarily entirely appropriate.

4.3. *Discussion on the Line-Shape of the Broad Component*

Outflow geometry is typically invoked to explain the line-shape of the emission lines tracing it. We consider reasonable geometries that conform to the line-shape and spatial extent of the broad component. From the spatial extent (Figure 3) the outflow seems to have a bi-conical or "disk-like" shape. If a radial outflow from the central star cluster is considered, then a bi-conical outflow seems to be the favored geometry. In the core of the galaxy, the width of the broad component is smallest and increases at larger radii, the opposite of what would be expected from a "disk-like" geometry where the core would show the broadest wings from seeing both gas components moving directly along the line of sight. The broad velocity offsets imply the upper bi-cone is angled away from the observer slightly while the lower bi-cone is consistent with being perpendicular to our line of sight. Increasing widths of the broad component at larger radii, however, are incompatible with both geometries assuming a simple radial outflow.

The gas in the broad component is likely not all traveling at the same speed and has a velocity distribution of its own in addition to how the velocities line up with the line of sight. Considering both effects, it is surprising that the line-shapes of the wings are so consistent across the entire wing region, which spans 4 spatially resolved beams along the vertical axis in Figure 4. If the Lorentzian profile is just a coincidence of geometry of the outflow, then it would be extremely unlikely to have the same line-shape across the whole wing region which is larger than the seeing and spans above and below the central starburst. Therefore, it seems likely that the mechanism behind the wing's line-shape needs to be a general phenomenon and should be independent of chance alignments of filaments of gas.

The effects of the outflow on the ionized gas kinematics can be seen in the velocity offset and width maps (Figure 4). Both velocity offset maps have a similar geometry with a redshifted component in the upper half of the field of view, but with different amplitudes, ∼4 km s^{-1} and ∼40 km s^{-1} for the narrow and broad respectively. In the context of an outflow, consistency in radial velocities could be due to the entrainment of cooler gas clouds by the higher velocity wind. As the wind moves outward, it interacts with the stationary, denser gas clouds by imparting some of its momentum to the stationary gas, effectively sweeping up the clouds into the flow. In this scenario, the motions of the denser clouds are not dominated by virial motion in the gravitational potential well. The velocity offset maps support this further as they do not show strong evidence of rotation. More likely, the starburst itself and the feedback it produces are the primary drivers of the kinematics seen in Pox 186.

We are unable to explain the enhancement in the narrow component velocity dispersion at the top and bottom of the field of view. Increasing uncertainties in the fit can partly explain the enhanced widths, but not completely. It is interesting, however, that this enhancement is seen at the "ends" of the elongated region where the broad component is detected (Figure 3). In the context of condensations of denser gas being blown out, this enhancement could be the eventual "evaporation"

or break-up of the dense cloud as it disperses into the low surface brightness component. This low surface brightness component could be indicative of ionized gas ejected from the galaxy, escape of ionizing radiation to large radii, or both. Unfortunately, we are unable to map the full spatial extent of the enhanced velocity dispersion around Pox 186.

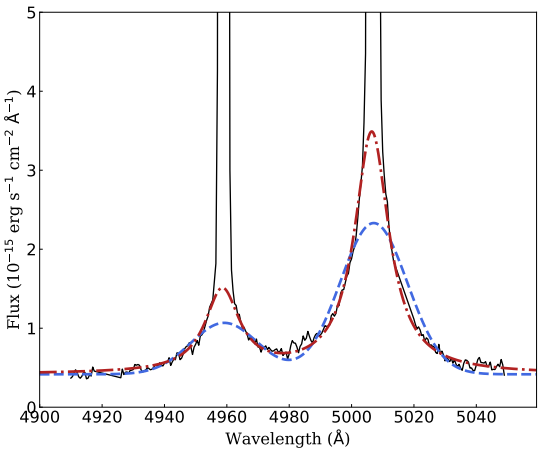


Figure 5. Broad component of [O III] in the wing region. The solid black line is the data, while the dashed blue line is the Gaussian fit, and the dot-dashed red line is the Lorentzian fit. A Lorentzian profile is significantly better at describing the broad component line shape and isn't as prone to underestimating the broad component flux as the Gaussian fit near the core of the line.

We use the summed spectrum of the "wing region" to explore the differences in the state of the high and low velocity gas by comparing the [O III](5007+4959)/Hβ ratio of the narrow component and the wing component separately. [O III]/Hβ is affected by the ionization parameter, metallicity, and density of the emitting gas making it particularly useful to qualitatively compare different gas components. We adopt the same fitting technique described in Section 2.2 and use a Lorentz profile convolved with the instrument response for the wings and a Gaussian in the core. The [O III]/Hβ ratios are 9.7 $\pm$ 5.7 in the wings and 8.3 $\pm$ 0.6 in the core. While these two ratios are consistent with one another at a 1σ level, with deeper data it is possible this discrepancy could be proven real. If so, it could provide insights into the mechanism behind the broad component such as an enhanced collision rate, higher ionization state, or be indicative of a metal enriched outflow.

4.4. *Outflows in Low-Mass Galaxies*

Catastrophic cooling has been proposed as a mechanism for creating the high O_{32} ratios and large [O III] luminosities seen in GPs (Silich et al. 2004; Oey et al. 2017; Jaskot et al. 2019). In low metallicity environments, the mechanical feedback from star formation is suppressed which allows for dense ionized gas clouds to stay closer to the star cluster without being driven outward and merged together. This is in contrast to when the dense clouds are blown out where they effectively create a shell around the starburst. These lower metallicity, denser clouds close to the starburst are extremely efficient at cooling (through [O III] primarily), and a side effect of not being blown out is that the high ionization, low density channels between clouds are preserved. Ionizing radiation and outflows driven by stellar processes escape through these channels.

At the interface between the low density channels and the higher density clouds, interactions between the two phases are expected. Schneider et al. (2020) showed this interaction is expected to transfer momentum from the low density winds to the high density clouds in the form of mixing. Turbulent mixing layers have commonly been proposed as an alternative mechanism for broad emission lines but it is especially attractive here due to the relative strengths of the two gas components and their homogeneity across the galaxy. In addition, the growth in velocity width of the broad component with increasing radii is consistent with entrainment of the relatively cool (T$\sim$10^4 K) gas into a fast moving, hot wind (Webster et al. 2001).

Figure 6 compares the calculated mass loading factor for Pox 186 with observations of other dwarf starburst galaxies and simulations. It is typically thought that low mass starburst galaxies tend to have higher mass-loading factors as their low mass makes it easier to blow gas out of their gravitational potential wells. Simulations (shown in black and grey in Figure 6) support this view (Vogelsberger et al. 2013; Ford et al. 2014; Muratov et al. 2015). Observations of mass-loading factors, however, vary over an order of magnitude depending on the phase of gas observed. McQuinn et al. (2019) (dark blue circles) measure mass-loading factors using Hα only and find no strong relationship with stellar mass. Rather, they find galaxies with highly concentrated star-formation tend to have higher mass-loading factors. Chisholm et al. (2017) (light blue crosses) use UV absorption lines of extreme starbursts, probing low and high ionization states, and find better agreement with simulations. However, these are still consistent with McQuinn et al. (2019) within the uncertainties.

We find Pox 186 to be markedly different from simulations, and more in line with mass-loading factors from McQuinn et al. 2019 (Figure 6). This is understandable as both mass-loading factors were derived from only Balmer recombination lines, thus only probing one gas

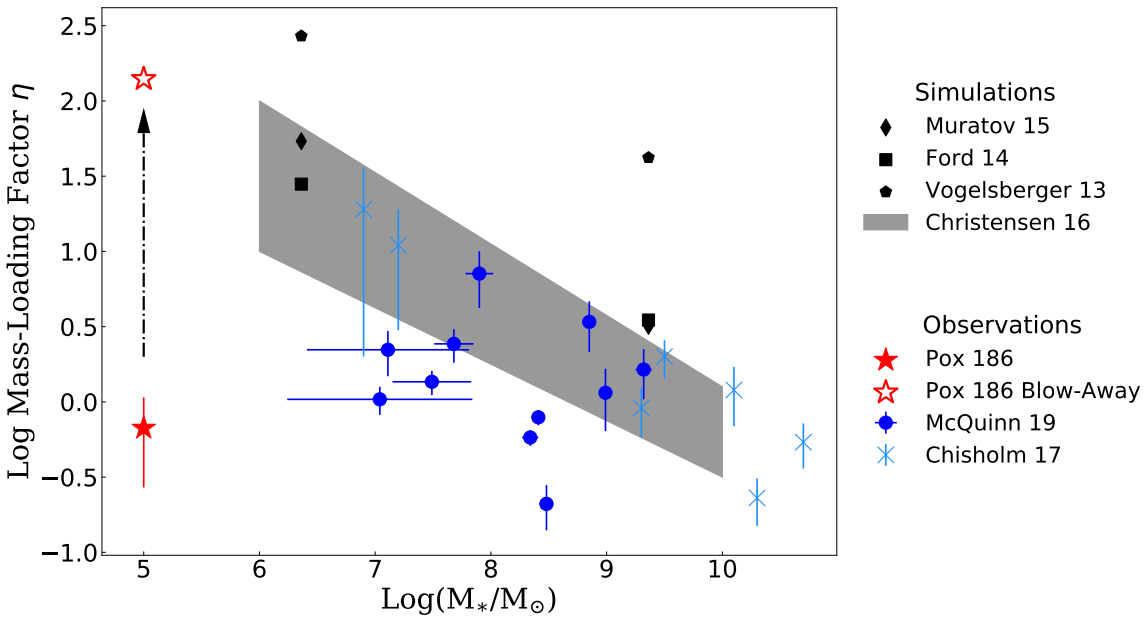


Figure 6. Mass-loading factors as a function of stellar mass. Both the observed mass-loading factor of Pox 186 (filled red star) and the mass-loading factor necessary to remove the expected H I mass from galaxy scaling relations (empty red star) are shown. For context, we include observations from McQuinn et al. (2019) shown with blue circles, and Chisholm et al. (2017) shown in light blue crosses. Simulation predictions are shown with the black diamonds (Muratov et al. 2015), squares (Ford et al. 2014), and pentagons (Vogelsberger et al. 2013). We also show the range of predictions from Christensen et al. (2016) with the grey shaded region.

phase. The difference between observations and simulations, however, is harder to explain. The results from Chisholm et al. (2017) suggest observing other phases could start to bring observed mass-loading factors in-line with simulations. In addition, measuring mass outflow rates require rough approximations in most cases. It seems unlikely, however, that the assumptions could make up for two orders of magnitude difference between Pox 186's mass-loading factor and what would be expected from simulations. Likewise, the non-detection in H I suggests that the mass-loading factor of the ionized gas in Pox 186 plays a more important role in the total mass loading factor than it may in a normal, more massive galaxy with a large reservoir of neutral gas (Roberts-Borsani 2020).

The observed suppressed mass-loading factor can also be the result of a blow-away that significantly depleted the reservoir of gas that can be loaded into the outflow. Corbin & Vacca (2002) found the central star-cluster to be 4±1.3 Myrs old using a stellar population synthesis model of single stellar populations with various ages assuming instantaneous star-formation. Using Starburst99 models (Leitherer et al. 1999) and continuous star formation increases this age to 6 Myrs. While 4 Myrs is young, there is enough time for supernovae to explode and drive significant outflows given that it only takes $\sim 10^5$ yrs for the wind, or $\sim 10^4$ yrs for supernova ejecta to reach the outer edge of Pox 186. We can estimate what the mass-loading factor would have been during the blow-away phase as follows: Assuming the stellar mass to H I mass scaling relation from Parkash et al. (2018), Pox 186 would have had $10^{7.2}$ $M_\odot$ in H I. Including this mass into the outflow over the last 4 Myrs would increase the mass-loading factor to 140, bringing it in line with the extrapolations from simulations at low masses. Therefore it is possible that a large fraction of the ISM has already been removed by stellar feedback and the suppressed mass-loading factor measured today is a consequence of a previous episode of gas removal.

In this regard, the simplistic assumption of a single-aged burst of star formation may be misleading us. Crowther (2019) provides a good overview of the 30 Dor star forming region in the LMC and promotes detailed study of this region as a guide to similar giant star forming complexes which, due to distance, cannot be observed in such detail. Because the individual stars in the 30 Dor region can be resolved both through imaging and spectroscopy, it is possible to develop an evolutionary history. Crowther (2019) summarizes that star formation in 30 Dor started 25 Myr ago and has proceeded up until at least 2 Myr ago. However, if 30 Dor were treated as typical for more distant star forming regions (i.e., as an instantaneous starburst) one would derive a considerably younger age.

4.5. *Pox 186 as a Green Pea Analogue*

In the Introduction, we put forward three observations supporting the view that Pox 186 is a nearby analogue of the Green Pea galaxies. Our kinematic study has provided a fourth line of evidence. In a spectroscopic study of six Green Pea galaxies, Amorín et al. (2012) found high velocity gas (FWZI $\geq$ 1000 km s^{-1}) in all of them. Together with the observation by Chisholm et al. (2017) that all Green Pea galaxies show evidence of outflows, it seems plausible that outflows are responsible for clearing pathways allowing for the large Lyman continuum escape fractions for the Green Pea galaxies. In support of this, in an IFU study of Mrk 71, a starburst hosted by the nearby galaxy NGC 2366 which has been deemed the nearest Green Pea analogue by Micheva et al. (2017), Micheva et al. (2019) also find a broad emission line component. Micheva et al. (2019) conclude that their "results strongly indicate that kinematical feedback is an important ingredient for LyC leakage in GPs." The characteristics of Mrk 71 show many similarities to Pox 186, including a "wing" of emission line gas. Thus, in all regards, Pox 186 can be considered as a nearby analogue to the Green Pea galaxies, albeit in a much lower mass regime.

5. CONCLUSIONS

Our new observations of Pox 186 have revealed a remarkable outflow of ionized gas, making a blow-away scenario increasingly likely. The broad component shows $\sim 5-10\%$ of the H II mass will be completely removed from the galaxy, while the updated distance using Cosmicflows-3 makes Pox 186 even smaller than previously thought. It is significant that such a small galaxy ($< 1.8\times 10^7$ M$_\odot$) is capable of producing a star-cluster of 10^5 M$_\odot$, but it remains unclear if the low mass is a result of the starburst blowing material out. Assuming this is true we find the mass-loading factor must be $\sim$140 to remove the starting reservoir of H I expected from dwarf galaxy scaling relations. Such a large amount of gas blown away from the galaxy should still be partly detectable as a halo of gas surrounding Pox 186, much like the low surface brightness component present in HST imaging (Corbin & Vacca 2002). Our field of view, however, restricts our ability to measure the mass in this component.

Using MCMC fitting we have investigated the kinematic properties of ionized gas as traced by [O III] in Pox 186. We find the [O III] doublet is well fit by a two component model: a strong, narrow, Gaussian component, and a fainter, broad, Lorentzian component. Across the entire field of view, the narrow component is present and its flux distribution follows the general light distribution in the galaxy as seen in broad band imaging, while the broad component is detected in an elongated region extending vertically that is distinct in shape from the narrow component and continuum. The broad component forms strong evidence for an outflow in Pox 186 with a velocity 4-14 times larger than the escape velocity. Our spatially resolved observations have shown a consistent line-shape across the region, implying some global mechanism is behind the formation of the broad component.

One promising model that simultaneously explains these observations is a scenario where the low density, hot (T$\sim 10^6$ K) central starburst outflow emanating from the galaxy flows around high density warm (T$\sim 10^4$ K) clouds where it mixes and imparts some of its momentum into the gas on the surface of the warm clouds. This mixing is what generates the broad wings in the ionized gas while the relatively untouched core of the clouds emit the narrow component.

This is not the only viable explanation, however, and follow-up observations are required to validate or refute this model. It is possible the wing component is due to a series of filaments, clouds, and shells of ionized gas with a velocity distribution that recreates the wings when projected along the line of sight. The consistency in line-shape of the broad component would then be an indication of an ISM that is relatively uniform. The value of this model is that it does not require an unseen phase of gas to be interacting all the time to recreate the observations. The ionized gas only needs periodic energy and momentum input from supernova of stars in the central star cluster.

To distinguish between these two scenarios and confirm or refute the interacting wind model one could look at a variety of indicators. First, imaging in the FUV and X-ray would immediately show whether a hot unseen wind phase is present and its radial distribution would indicate whether some of its energy and momentum is being lost to the warm ionized gas. Second, the turbulent mixing of ionized gas would act to increase the local magnetic field strength. Chakraborti et al. (2012) find increased magnetic field strengths in GPs and suggest their magnetic fields could induce large star-formation events, but in a turbulent mixing scenario it could go the other way as well. Synchrotron emission in the radio regime or polarization observations could be used to measure the magnetic field strength across the galaxy that would then be compared with the strength of the broad emission. If the wings are indeed the product of mixing then one would expect increased magnetic field strengths to be correlated with increasing wing strength.

As a final remark we re-emphasize the unique qualities of Pox 186. The majority of the first galaxies that formed were likely similar to Pox 186 in mass, being about the size of giant H II regions today, and, like Pox 186 seems to have done, formed in isolation. Pox 186 offers the closest example of such a galaxy and is a potential local laboratory to study the extreme ISM properties of the low-mass star-forming galaxies during the early universe.

Acknowledgments: We would like to thank Michele Guala for his insight into turbulent flows, and Kristen McQuinn and John Cannon for providing their data used in this paper. This research made use of NASA/IPAC Extragalactic Database (NED) and NASA's Astrophysical Data System. We also express gratitude to the Gemini Help Desk, which assisted the reduction process. We thank the anonymous referee for their comments which led to significant improvements in our paper.

REFERENCES

Amorín R. et al., 2012b, ApJ, 754, L22
Andersson E. P., Agertz O., Renaud F., 2020, MNRAS, 494, 3328
Begum, A., & Chengalur, J. N. 2005, MNRAS, 362, 609
Cardamone, C., Schawinski, K., Sarzi, M., et al. 2009, MNRAS, 399, 1191
Chakraborti, S., Yadav, N., Cardamone, C., & Ray, A. 2012, ApJL, 746, L6
Chisholm, J., Tremonti, C., Leitherer, C., & Chen, Y. 2017, MNRAS, 469, 4831
Chisholm, J., Tremonti, C., Leitherer, C., 2018, MNRAS, 487, 1690
Christensen, C. R., Davé, R., Governato, F., et al. 2016, ApJ, 824, 57
Christensen, C. R., Davé, R., Brooks, A., Quinn, T., & Shen, S. 2018, ApJ, 867, 142
Corbin, M. R., & Vacca, W. D. 2002, ApJ, 581, 1039
Crowther, P. A. 2019, Galaxies, 7, 88
Dekel, A., & Silk, J. 1986, ApJ, 303, 39
Ferrara, A., & Tolstoy, E. 2000, MNRAS, 313, 291
Finkelstein, S. L., Ryan, R. E., Jr., Papovich, C., et al. 2015, ApJ, 810, 72
Finkelstein, S. L., D'Aloisio, A., Paardekooper, J.-P., et al. 2019, ApJ, 879, 36
Ford, A. B., Davé, R., Oppenheimer, B. D., et al. 2014, MNRAS, 444, 1260
Foreman-Mackey D., Hogg D. W., Lang D., Goodman J., 2013, PASP, 125, 306
Genzel, R., Newman, S., Jones, T., et al. 2011, ApJ, 733, 101
Guseva, N. G., Papaderos, P., Izotov, Y. I., Noeske, K. G., & Fricke, K. J. 2004, A&A, 421, 519
Heckman, T. M., Alexandroff, R. M., Borthakur, S., Overzier, R., & Leitherer, C. 2015, ApJ, 809, 147
Hopkins, P. F., Quataert, E., & Murray, N. 2012, MNRAS, 421, 3522
Hu, C.-Y. 2019, MNRAS, 483, 3363
Izotov, Y. I., Orlitov á, I., Schaerer, D., et al. 2016a, Nature, 529, 178
Izotov, Y. I., Schaerer, D., Thuan, T. X., et al. 2016b, MNRAS, 461, 3683
Izotov, Y. I., Thuan, T. X., & Guseva, N. G. 2017, MNRAS, 471, 548
Izotov Y. I., Worseck G., Schaerer D., Guseva N. G., Thuan T. X., Fricke A. V., Orlitová I., 2018b, MNRAS, 478, 4851
Jaskot, A. E., & Oey, M. S. 2013, ApJ, 766, 91
Jaskot, A. E., Dowd, T., Oey, M. S., et al. 2019, ApJ, 885, 96
Kennicutt R. C., 1998, ApJ, 498, 541
Kim, C.-G., Ostriker, E. C., & Raileanu, R. 2017, ApJ, 834, 25
Kourkchi et al. 2020, AJ, 159, 67
Kunth, D., Sargent, W. L. W., & Kowal, C. 1981, A&AS, 44, 229
Kunth, D. & Sargent, W. L. W. 1983, ApJ, 273, 81. doi:10.1086/161350
Kunth, D., Maurogordato, S., & Vigroux, L. 1988, A&A, 204, 10
Leitherer, C., et al. 1999, ApJS, 123, 3
Livermore R. C., Finkelstein S. L., Lotz J. M., 2017, ApJ, 835, 113
Lu, Y, Benson, A., Wetzel, A., et al. 2017, ApJ, 846, 66
Mac Low, M., & Ferrara, A. 1999, ApJ, 513, 142
Madau P., Pozzetti L., Dickinson M., 1998, ApJ, 498, 106
Marlowe A. T., Heckman T. M., Wyse R. F. G., Schommer R., 1995, ApJ, 438, 563
Martin, C. L. 1999, ApJ, 513, 156
McQuinn, K. B. W., van Zee, L., & Skillman, E. D. 2019, ApJ, 886, 74
Micheva, G., Oey, M. S., Jaskot, A. E., & James, B. L. 2017, ApJ, 845, 165
Micheva, G., Christian Herenz, E., Roth, M. M., et al. 2019, A&A, 623, A145.

Muratov, A. L., Keres, D., Faucher-Giguére, C.-A., et al. 2015, MNRAS, 454, 2691
Naidu R. P., Tacchella, S., Mason, C. A., Bose, S., Oesch, P. A., Conroy, C., 2020, ApJ, 892, 109
Nelson, D., Pillepich, A., Springel, V., et al. 2019, MNRAS, 490, 3234
Oey, M. S., Herrera, C. N., Silich, S., Reiter, M., James, B. L., Jaskot, A. E., & Micheva, G. 2017, ApJL, 849, L1
Oñorbe, J., Boylan-Kolchin, M., Bullock, J. S., et al. 2015, MNRAS, 454, 2092
Oppenheimer, B. D., & Davé, R. 2009, MNRAS, 395, 1875
Osterbrock, D. E. & Ferland, G. J. 2006, The Astrophysics of Gaseous Nebulae and Active Galactic Nuclei (Mill Valley: University Science Books)
Parkash, V., Brown, M. J. I., Jarrett, T. H., Bonne, N. J. 2018, ApJ, 864, 40
Roberts-Borsani, G. W. 2020, MNRAS, 494, 4266
Robertson B. E., Ellis R. S., Furlanetto S. R., Dunlop J. S., 2015, ApJ, 802, L19
Sargent, W. L. W., Young, P. J., Boksenberg, A. and Tytler, D. 1980, ApJ, *Suppl.*, 42, 41
Schaerer, D., Izotov, Y. I., Verhamme, A., et al. 2016, A&A, 591, L8
Schlafly, E. F. & Finkbeiner, D. P., 2011, ApJ, 737, 103
Schneider, E. E., Ostriker, E. C., Robertson, B. E., Thompson, T. A., 2020 preprint (arXiv:2002.10468)
Silich, S., Tenorio-Tagle, G., & Rodrígues-González, A. 2004, ApJ, 610, 226
Shaya et al. 2017, ApJ, 850, 207
Steidel, C. C., Bogosavljevi ć, M., Shapley, A. E., et al. 2018, ApJ, 869, 123
Verhamme, A., Orlitov á, I., Schaerer, D., et al. 2017, A&A, 597, A13
Vogelsberger, M., Genel, S., Sijacki, D., et al. 2013, MNRAS, 436, 3031
Webster, D. R., Roberts, P. J. W., Raád, 2001, Experiments in Fluids, 30, 65
Weisz, D. R., & Boylan-Kolchin, M. 2017, MNRAS, 469, L83
Yang, H., Chu, Y.-H., Skillman, E. D., & Terlevich, R. 1996, AJ, 112, 146
Young, P. J., Sargent, W. L. W., and Boksenberg, A. 1982b, ApJ, *Suppl.*, 48, 455
Zuo L., Lu L., 1993, ApJ, 418, 28

APPENDIX

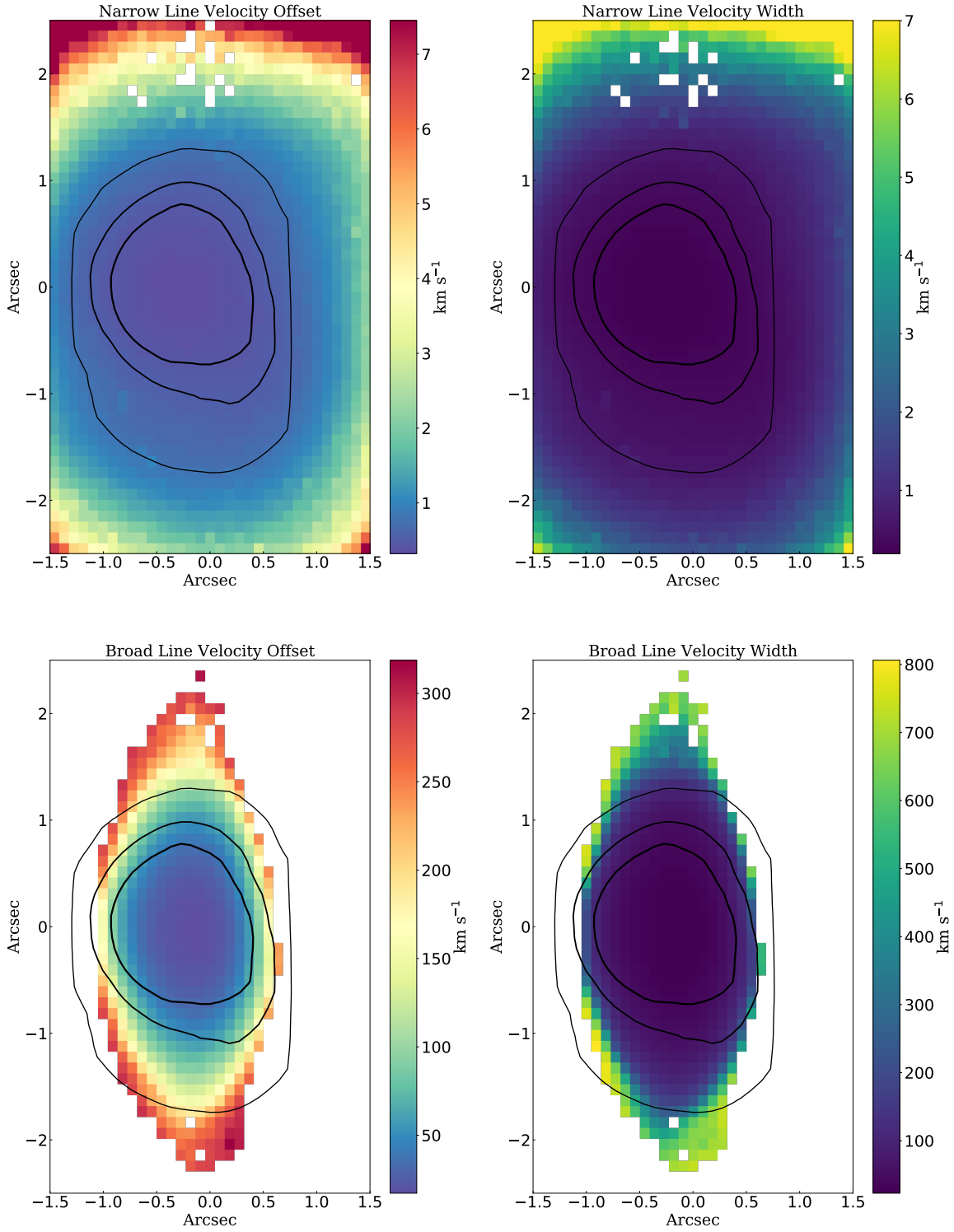


Figure 7. Uncertainties in the kinematics of the two Gaussian components derived from the parameter distribution of two-Gaussian model fit described in Section 2. The uncertainties shown are the mean of the upper and lower 1σ widths of the parameter distributions.

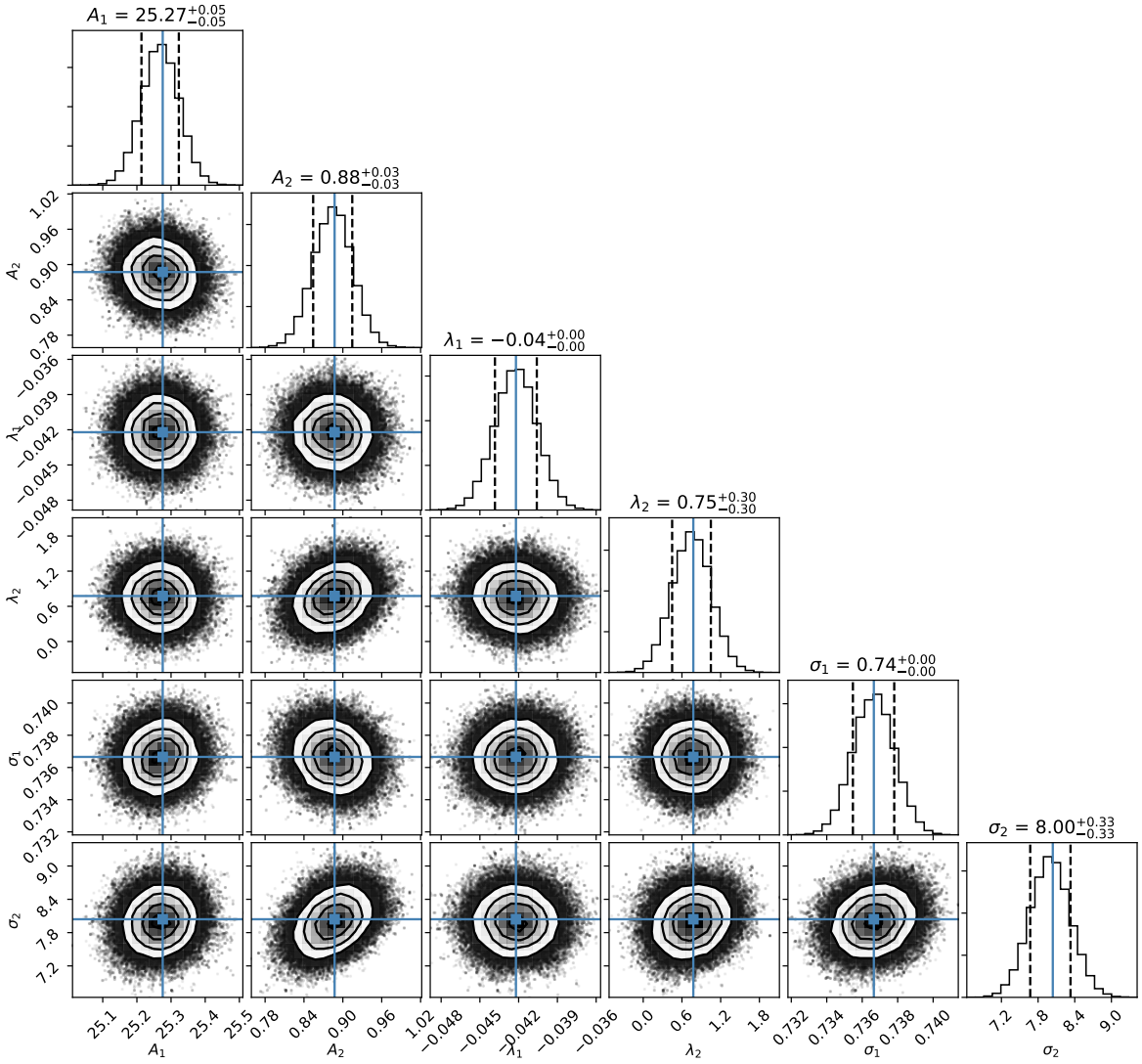


Figure 8. One and two dimensional projections of the posterior probability distribution for the Gaussian widths (σ), line center offsets (λ), and line fluxes (A). The blue lines denote the median of the distributions with the dashed black lines showing the 16% and 84% quantiles. The degeneracies between the two components were overcome by restricting the prior range of the amplitude for the broad component. Note: This is a fit to the central, brightest pixel.